NeuroImage 200 (2019) 590–600

Contents lists available at ScienceDirect

NeuroImage

journal homepage: www.elsevier.com/locate/neuroimage

Functional imaging of rostrocaudal spinal activity during upper limb motor tasks

Nawal Kinany [a,b,c,*], Elvira Pirondini [b,c], Roberto Martuzzi [d], Loan Mattera [d], Silvestro Micera [a,e,1], Dimitri Van de Ville [b,c,1]

[a] Bertarelli Foundation Chair in Translational Neuroengineering, Center for Neuroprosthetics, Institute of Bioengineering, École Polytechnique Fédérale de Lausanne (EPFL), Lausanne, 1015, Switzerland
[b] Medical Image Processing Laboratory, Center for Neuroprosthetics, Institute of Bioengineering, École Polytechnique Fédérale de Lausanne (EPFL), Lausanne, 1015, Switzerland
[c] Department of Radiology and Medical Informatics, University of Geneva, Geneva, 1211, Switzerland
[d] Fondation Campus Biotech Genève, 1202, Geneva, Switzerland
[e] Translational Neural Engineering Area, The Biorobotics Institute, Scuola Superiore Sant'Anna, Pisa, 56025, Italy

ARTICLE INFO

Keywords:
Functional MRI
Spinal cord
Motor task
Upper limb
Electromyography

ABSTRACT

The spinal cord is the main interface between the brain and the periphery. It notably plays a central role in motor control, as spinal motoneurons activate skeletal muscles involved in voluntary movements. Yet, the spinal mechanisms underlying human movement generation have not been completely elucidated. In this regard, functional magnetic resonance imaging (fMRI) represents a potential tool to probe spinal cord function non-invasively and with high spatial resolution. Nonetheless, a thorough characterization of this approach is still lacking, currently limiting its impact. Here, we aimed at systematically quantifying to which extent fMRI can reveal spinal cord activity along the rostrocaudal direction. We investigated changes in the blood oxygenation level dependent signal of the human cervical spinal cord during bimanual upper limb movements (wrist extension, wrist adduction and finger abduction) in nineteen healthy volunteers. Prior to scanning, we recorded the muscle activity associated with these movements in order to reconstruct the theoretical motor-pool output pattern using an anatomy-based mapping of the electromyographic (EMG) waveforms. EMG-derived spinal maps were characterized by distinct rostrocaudal patterns of activation, thus confirming the task-specific features of the different movements. Analogous activation patterns were captured using spinal cord fMRI. Finally, an additional fMRI dataset was acquired from a subset of the participants (n = 6) to deploy a multivoxel pattern analysis, which allowed successful decoding of movements. These combined results suggest that spinal cord fMRI can be used to image rostrocaudal activation patterns reflecting the underlying activity of the motoneuron pools innervating the task-related muscles. Spinal cord fMRI offers the prospect of a novel tool to study motor processes and potentially their modification following neurological motor disorders.

1. Introduction

More than a simple relay, the spinal cord plays a crucial role in movement generation and control (Alstermark and Isa, 2012; Giszter et al., 2012; Vahdat et al., 2015) and can be functionally affected in neurological motor disorders, such as spinal cord injury or multiple sclerosis. Yet, tools to directly and non-invasively investigate the nature and function of the underlying spinal mechanisms in humans are still lacking.

To date, studies assessing spinal cord function in humans have mainly relied on indirect peripheral measurements (muscle activity or force, reflexes, sensory tests, etc.). Notably, muscle recordings have been used to indirectly infer spinal activity during movements by reconstructing theoretical spatiotemporal motoneural activation maps (i.e., 'spinal maps'), using a combination of the acquired electromyographic (EMG) signals with anatomical knowledge of muscle innervation (Yakovenko

* Corresponding author. Bertarelli Foundation Chair in Translational Neuroengineering, Center for Neuroprosthetics, Institute of Bioengineering, École Polytechnique Fédérale de Lausanne (EPFL), Lausanne, 1015, Switzerland.
E-mail address: nawal.kinany@epfl.ch (N. Kinany).
[1] Silvestro Micera and Dimitri Van De Ville contributed equally to this work.

https://doi.org/10.1016/j.neuroimage.2019.05.036
Received 31 January 2019; Received in revised form 12 May 2019; Accepted 13 May 2019
Available online 17 May 2019

et al., 2002). These spinal maps have been extensively used to explore spinal motor output in healthy humans (e.g., Cappellini et al., 2010; Ivanenko et al., 2006, 2013, during locomotion, Pirondini et al., 2016, during reaching movements), or also to illustrate disrupted motor pathways (e.g., Grasso et al., 2004, in spinal cord injured patients, Coscia et al., 2015, in stroke patients). Nevertheless, this technique relies solely on anatomy-based mapping of muscle outputs. For that reason, it is merely an indirect estimation of the spinal cord activity and it does not fully elucidate the underlying mechanisms.

In this context, functional magnetic resonance imaging (fMRI) of the spinal cord stands as a promising tool to directly and non-invasively investigate spinal processes involved in voluntary movements (Wheeler-Kingshott et al., 2014). In the brain, this technique is already widely deployed, to understand motor control as well as to capture neural signatures of clinical conditions. Relying on the same principle (i.e., the blood oxygenation level dependent – BOLD – signal), spinal cord fMRI measures signal changes reflecting spinal neural activity, in spite of additional technical difficulties inherent to the region of interest (e.g., small structure, field inhomogeneities, physiological noise) (Giove et al., 2004). Since the seminal work of Yoshizawa in 1996 (Yoshizawa et al., 1996), several studies have indeed confirmed the potential of spinal cord fMRI to monitor task-related activity, mainly with tasks involving the upper extremities (e.g., Backes et al., 2001; Bouwman et al., 2008; Govers et al., 2007; Madi et al., 2001; Maieron et al., 2007; Ng et al., 2008; Stroman and Ryner, 2001), but also during active and passive ankle movements (Kornelsen and Stroman, 2004, 2007).

However, technological limitations in the formerly available acquisition and processing methods (e.g., low field strength, no correction of physiological noise, no registration to a common template) have initially hindered the development of this approach. As a matter of fact, most early studies were mainly qualitative reports, hence limiting their potential applications, notably to clinical investigations (Kornelsen and Mackey, 2010). In comparison, a few recent works have leveraged novel advanced acquisition and processing paradigms to systematically assess spinal cord activity recorded with fMRI. For instance, these advances allowed confirmation of the robust lateralization of the cervical signal during unimanual isometric contractions (Weber et al., 2016b).

Here, we aim at further investigating the organization of spinal cord activity during voluntary movements, so as to better apprehend the potentials and limitations of the current spinal cord fMRI techniques. We believe that these evaluations represent a pivotal step to further develop spinal cord fMRI and potentially extend it to clinical investigations. Specifically, we want to systematically analyze cervical activations during different movements as regards to their distribution in the rostrocaudal direction. Indeed, during movement generation, spinal motoneurons (i.e., lower motoneurons), which are distributed over different spinal levels, act as an interface between upper motoneurons located in the motor cortex and skeletal muscles (Marieb and Hoehn, 2014). Thus, movements requiring activations of different muscles should be characterized by distinct spinal activation patterns.

So far, only one early study has investigated the potential of fMRI to reveal these distinct rostrocaudal activation patterns associated with different movements (Madi et al., 2001). In their study, Madi et al. probed BOLD signal changes, in three to six subjects, during three upper limb movements (elbow flexion, wrist extension and finger abduction, thus involving different myotomes) and observed activity at the site of muscle innervation, despite unexpected signal in other spinal segments. Notwithstanding the qualitative nature of the obtained results, this study provided a valuable insight into the potential of fMRI to capture the complexity of spinal cord functional activity in humans.

In our study, we extended this preliminary investigation to a more systematic analysis of rostrocaudal functional activity, in a larger cohort of subjects, during distal upper limb movements (wrist extension, wrist adduction and finger abduction). Those movements were selected to include different myotomes, whose rostro-caudal locations vary from C5 to T1. To systematically explore these activation patterns, we capitalized on advances in fMRI acquisition (e.g., higher field strength and selective field-of-view imaging (Finsterbusch, 2013)) and processing (e.g., slice-wise motion correction (Cohen-Adad et al., 2009; De Leener et al., 2017), physiological noise correction (Eippert et al., 2017) and normalization to a common template (De Leener et al., 2018)). Prior to fMRI acquisitions, muscular activity was also recorded to characterize the motoneuron output by means of EMG-derived spinal maps, so as to obtain theoretical estimations of the rostrocaudal activations, further compared to the acquired fMRI-derived spinal maps. Finally, we complemented our analysis pipeline with a multivariate statistical approach (i.e., multivoxel pattern analysis – MVPA), so as to fully exploit the information content of distributed patterns of spinal activity as well as to probe their precision and stability (Pereira et al., 2009).

Our results show that BOLD activity presented a distinct rostrocaudal cervical organization associated to the different upper limb movements, similar to the one inferred by anatomy-based mapping. Moreover, the subject-specific maps allowed decoding of performed motor tasks with high accuracy, confirming the task-specificity of BOLD spinal signals. These combined results allow highlighting the potential of spinal cord fMRI, and pave the way towards localized observation of human spinal cord function during disparate motor actions. We foresee that such straight measures of spinal neural activity could shed light on mechanisms disrupting motor pathways in neurological conditions. This could eventually lead to the development of new spinal biomarkers, hence complementing current peripheral and anatomical approaches.

2. Methods

2.1. Participants

Nineteen right-handed healthy subjects (11 females, 26.9 ± 3.4 years old) were enrolled in the study. Two participants had to be excluded from further analyses (see 3.1). All participants gave their written informed consent to participate, and the study had been approved by the Commission Cantonale d'Ethique de la Recherche Genève (CCER, Geneva, Switzerland, 2016-01566). All volunteers had normal or corrected-to-normal vision and no history of neurological disorders.

2.2. Experimental protocols

EMG and fMRI data were acquired during the same experimental session, which was divided into two phases (Fig. 1A): (1) Phase 1, in the mock scanner, serving both as training and to record EMG activity; (2) Phase 2, in the MRI scanner, to record spinal functional activity using fMRI.

Six of the subjects (3 females, 28 ± 1.7 years old) participated in an additional experimental session (i.e., Phase 3), during which only fMRI was performed, with a protocol adapted for Multivoxel Pattern Analysis (MVPA) (Coutanche and Thompson-Schill, 2012).

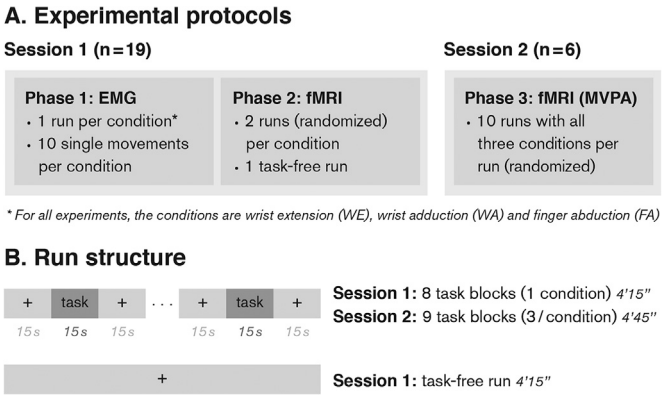

Fig. 1. | **Protocols** | **A.** Overview of the experimental recordings **B.** Schematic presentation of the structure of the runs.

2.2.1. Phase 1: EMG experiment

At the beginning of the first experimental session, the different bilateral movements were presented to the participants: wrist extension (i.e., wrist towards the top), wrist adduction (i.e., wrist towards the outside, with an ulnar deviation) and finger abduction (i.e., fingers spreading with thumb adducted). These movements were selected to include different myotomes, in order to potentially elicit activations in different spinal segments (Kendall et al., 2005). Subjects were asked to keep their fingers as relaxed as possible during the wrist movements, and to focus on their muscle activations throughout the experiment.

After appropriate training (i.e., when all movements were performed consistently by the subjects), subjects were installed in a mock scanner (a realistic magnet-free model of the actual MRI scanner) in supine position, with their hands relaxed on their thighs and the palm facing downwards. Phase 1 was subdivided into two parts during which the subjects were asked to perform the movements bilaterally following two paradigms (Fig. 1A – Phase 1). The first paradigm was designed as a *block experiment* with 8 blocks of movement alternated with 9 blocks of rest (Fig. 1B). Each block lasted 15 s, with an entire run lasting 4 min and 15 s. Instructions were displayed on a screen (fixation cross '+' during the rest blocks and text indicating 'movement repetitions' during the task blocks). Auditory cues were provided to inform the subjects of the different blocks. During the task blocks, subjects executed dynamic repetitions of the movements, prompted by the auditory cues (i.e., tones at a rate of ~0.5 Hz, so that 8 movements were performed per task block). Subjects were instructed to remain as still as possible during the rest blocks. One run was done for each movement type (i.e., three runs in total, with only one movement type performed during each run) and the order of the runs was randomized across participants. The second paradigm, instead, was a *single movement experiment* where movements were executed with only one repetition at a time (e.g., one bilateral wrist extension and back to the resting position) lasting approximately 2 s. For each repetition (i.e., each single movement), an auditory instruction was given by the experimenter to indicate the movement type to be performed. In total, each movement was repeated ten times, in a pseudo-randomized manner. This second paradigm was specific to the EMG experiment and not used in the MRI scanner (see 2.2.2).

2.2.2. Phase 2: fMRI characterization experiment

During functional acquisitions, the participants were installed in the MRI scanner in supine position. The experimental setup was identical to the one used in the mock scanner (visual and auditory cues) and the paradigm was the same as the *block experiment* in Phase 1. Each subject executed two runs of each movement, in a randomized manner (i.e., six runs in total, with only one movement type performed during each run, in blocks, see Fig. 1A – Phase 2). A task-free run (i.e., without any overt task) of the same duration as a task run was acquired at the beginning of the experiment (Fig. 1B). All runs (task and task-free) lasted 4 min and 15 s. Throughout the recordings, subjects were instructed to relax, breathe normally and minimize motion of the neck, head and shoulders. Movement execution was monitored using a camera. The goal of this monitoring was to ensure that subjects were performing the requested movement type for each run or block. In the event of an error, the fMRI acquisition was stopped and started again with the right movement type.

2.2.3. Phase 3: fMRI multivoxel pattern analysis experiment

In order to confirm the reliability of the fMRI activations elicited during Phase 2 and to further emphasize the task-specific characteristics of the spinal activation maps, an additional dataset was obtained (Fig. 1A – Phase 3). The experimental design was optimized for MVPA (i.e., many short runs including all three movements (Coutanche and Thompson-Schill, 2012)). Six of the initial subjects participated in this additional phase in the MRI scanner, where the same three movements had to be performed. The experiment was divided into ten runs, each including nine blocks alternated with rest, with each movement repeated three times in a randomized manner (Fig. 1B). Similarly to the previous session, movements were performed in blocks of 15 s and with 8 movement repetitions within each block (i.e., ~0.5 Hz). Each run lasted 4 min and 45 s.

2.3. EMG acquisition and preprocessing

During Phase 1, EMG recordings were performed on 15 arm and hand muscles (biceps brachii long head, BICL, triceps brachii long head, TRIC, brachialis, BRA, brachioradialis, BRAD, pronator teres, PRO, extensor carpi radialis, EXCR, extensor carpi ulnaris, EXCU, extensor digitorum communis, EXDC, flexor carpi radialis, FLCR, flexor carpi ulnaris, FLCU, flexor digitorum superficialis, FLDS, abductor digiti minimi, ABDM, extensor pollicis brevis, EXPB, adductor pollicis transversus, ADPT, abductor pollicis brevis, ABPB). EMG signals were acquired using a Noraxon Desktop DTS wireless system and superficial Ag–AgCl electrodes (Kendall H124SG, ECG electrodes 30×24 mm) placed on the above-mentioned muscles of the right upper limb, after appropriate skin preparation. EMG signals were sampled at 1500 Hz. The quality of the EMG signals was visually assessed throughout the recordings (e.g., noise, cross-talk between muscles, etc.). Before the beginning of the experiment, a Maximum Voluntary Contraction (MVC) test was performed for each muscle. This test consists in isometric contractions against resistance, repeated three times for each muscle and alternated with breaks to prevent muscle fatigue.

All raw EMG signals were first detrended and high-pass filtered at a frequency of 50 Hz (Butterworth filter, 7th order). Signals were then rectified and low-pass filtered at a frequency of 10 Hz (Butterworth filter, 7th order). Finally, they were normalized to the MVC value of each muscle (obtained after preprocessing of the related EMG signals), to allow comparison between subjects and movements. All processing steps were performed using Matlab (versions 2016a and 2017b, MathWorks, Natick MA).

2.4. EMG analysis

2.4.1. EMG-based estimation of spinal activity

EMG-derived spinal maps provide an anatomy-based estimation of the spatiotemporal activation of lower motoneurons in the spinal cord (Yakovenko et al., 2002). They are based on a combination of EMG recordings with knowledge of the rostrocaudal location of motoneurons pools innervating different muscles, hence providing the theoretical spinal cord output, without relying on direct imaging. For each spinal segment, we used a weighted summation of the preprocessed EMG envelopes (Fig. 2A), based on the weight coefficients summarized by Kendall et al. (2005), derived from empirical human studies, for the spinal levels C5 to T1 (Table S1). For the block experiment, EMG data were first segmented into individual repetitions (i.e., 8 repetitions for each block, thus 64 repetitions per movement type). For each movement, EMG-derived spinal maps were then computed for each repetition and averaged. Group spinal maps were obtained for each movement type by averaging over participants. In addition, the stability of the EMG-derived spinal maps across movements was estimated for each participant by computing the average Pearson's correlation coefficients between the 64 repetitions. In order to relate EMG-derived and fMRI-derived activation maps, the group-level EMG-derived spinal maps obtained from the block experiment were averaged over time and interpolated (spline interpolation) to generate one-dimensional projections along the z dimension (i.e., spinal levels). These projections were then compared to the fMRI-derived projections using Pearson's correlation coefficients.

2.4.2. Subject-wise classification of estimated spinal maps

In order to confirm the task-specific characteristics of the rostrocaudal activations patterns derived using EMG, a classifier (Linear Discriminant Analysis, LDA) was designed for each subject to discriminate across the three movements using the EMG-derived spinal maps from the *single movement experiment* (i.e., ten repetitions). For the *single*

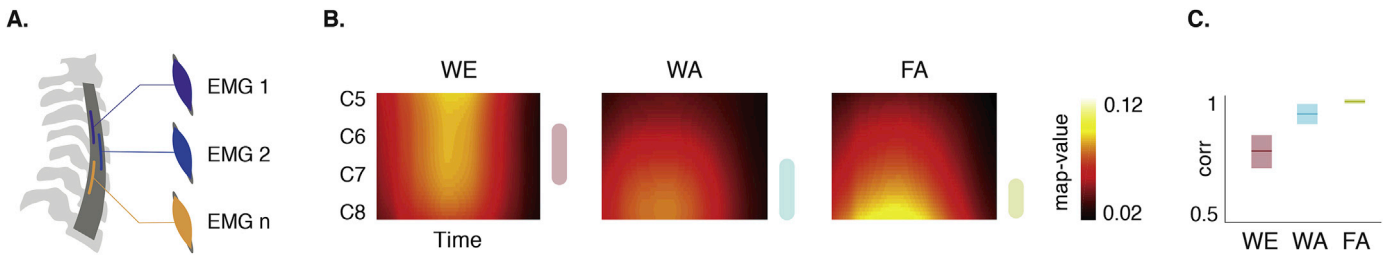

Fig. 2. | **Characterization of rostrocaudal spinal activation patterns (EMG)** | **A.** EMG-derived spinal maps are used to estimate the spatiotemporal activation of lower motoneurons in the spinal cord (Yakovenko et al., 2002). The motor-pool output patterns are computed using a weighted summation of the EMG signals from the 15 recorded muscles, based on knowledge about the rostrocaudal locations of the motoneuron pools innervating those muscles (see Table S1). **B.** Group EMG-derived spinal maps for the different movements (WE = wrist extension, WA = wrist adduction, FA = finger abduction). Spinal maps were averaged over subjects and repetitions (64 repetitions of each movement for each subject). The color bars, displayed at the right of each map, represent the a priori expected peaks of activation. Spinal levels are displayed on the *y*-axis, and *x*-axis corresponds to the duration of the movement (~2 s). **C.** Correlation between the time-averaged EMG-derived spinal maps of the different movement repetitions. Data are presented as mean over subjects ± SE.

movement experiment, EMG-derived spinal maps were computed as above, independently for each repetition. We used as features the activity of the EMG-derived spinal maps from C5 to T1 averaged over time. The average discards the temporal component of the EMG-derived spinal maps, but allows comparison with the fMRI-MVPA results, where beta images are used as inputs. A three-class LDA classifier was employed (same covariance matrix for each class), with leave-one-movement-out cross validation, within each subject (for the sake of comparison, only the six subjects who performed the MVPA experiment were considered). Confusion matrices were computed considering all cross validation folds, to summarize the accuracy of the classification. In order to assess the statistical significance of those results, we performed non-parametric permutation tests. Specifically, we built 1000 classifiers for each subject, with randomly assigned labels at each permutation fold (i.e., same labels for all subjects within the same permutation), and computed confusion matrices for each permutation and subject. For each permutation, the mean overall accuracy over subjects was calculated and the 99th percentile of this null distribution was defined to obtain the threshold for significance ($p = 0.01$).

2.5. fMRI acquisition and preprocessing

2.5.1. Imaging protocol

Imaging data were acquired with a 3.0 T S Prisma scanner (Erlangen, Germany), equipped with a 64-channel head (only inferior element, HC7, was used) and neck coil (both anterior and posterior elements, NC1 and NC2, were used – i.e., 24 channels). For the MVPA recordings, a soft cervical collar was employed to stabilize the neck. All functional acquisitions were performed with a gradient-echo echo-planar sequence, with ZOOMit selective field-of-view imaging (Repetition Time (TR) = 2.5 s, Echo Time (TE) = 34 ms, FOV = 48 × 144 mm, flip angle = 80°, in-plane resolution = 1 × 1 mm, slice thickness = 3 mm). A similar sequence was used by Weber and colleagues (Weber et al., 2016b) and allowed to efficiently observe spinal activation during isometric wrist movements. 32 axial slices were acquired for each volume, covering the cervical enlargement. Before acquisition, shimming adjustments focused on the spinal cord were carried out to optimize the magnetic field homogeneity. In Session 1, 102 vol were acquired (scan duration of 4 min and 15 s), while 114 vol were acquired for Session 2 (scan duration of 4 min and 45 s). A high-resolution T2-weighted anatomical image, covering C1 to T6 vertebra, was also acquired with a SPACE sequence (single slab 3D turbo spin echo sequence with a slab selective, variable excitation pulse, TR = 1500 ms, TE = 135 ms, echo train length = 74, flip angle = 140°, resolution = 0.4 × 0.4 × 0.8 mm, sagittal orientation).

All preprocessing steps were performed using the Oxford Center for fMRI of the Brain's (FMRIB) Software Library (FSL, version 5.0) (Jenkinson et al., 2012) and the Spinal Cord Toolbox (SCT, version 3.2.1) (De Leener et al., 2017).

2.5.2. Motion correction

As the spinal cord is a very small structure, motion correction is a crucial step to increase the temporal signal-to-noise ratio (tSNR). Motion correction was performed in two steps: i) slice-wise realignment, to account for the articulated structure of the spine (Cohen-Adad et al., 2009; De Leener et al., 2017); and ii) motion scrubbing (Power et al., 2014). For the slice realignment, all images were visually inspected to rule out the presence of artifacts and cropped to remove bottom slices with insufficient signal (the number of removed slices ranges from 3 to 8 across subjects and runs). Then, the volumes of each functional run were averaged and the centerline of the spinal cord was automatically extracted from the resulting image. A cylindrical mask with a diameter of 30 mm along this centerline was drawn and further used to exclude regions outside the spinal cord from the motion correction procedure, as those regions may move independently from the cord. Slice-wise realignment was performed using the mean functional image as the target image. The amount of motion was assessed by computing the average absolute value of the framewise displacement (FD), as well as the Pearson's correlation coefficients between the movement parameters and the task paradigm. Finally, all runs were aligned to the task-free run with FLIRT (FMRIB's Linear Image Registration Tool), using six degrees-of-freedom rigid-body transformations with spline interpolation and a normalized correlation cost function (Jenkinson et al., 2002). Motion scrubbing was subsequently performed by including outlier volumes as noise regressors during the GLM analysis (see 2.6.1). Outliers were detected with FSL's dedicated tool and using DVARS (i.e., the root mean square intensity difference of volume N to volume N+1) with a box-plot cutoff (75th percentile + 1.5 × the interquartile range) (Power et al., 2014). This metric was computed within the spinal cord mask (see 2.5.5). On average, two volumes per run were considered as outliers.

2.5.3. Physiological noise correction

The close proximity of the lungs, the heart and other visceral organs is an important source of motion when performing spinal cord fMRI (Brooks et al., 2008; Eippert et al., 2017; Piché et al., 2009). Moreover, cardiac activity generates a pulsatile flow in the cerebrospinal fluid (CSF) around the spinal cord, hence urging the need for physiological noise correction. Therefore, we recorded physiological signals during the functional acquisitions using a photoplethysmograph and a respiratory belt (Biopac MP150 system, California, USA). In order to ensure proper synchronization, the scanner triggers were simultaneously recorded. The physiological recordings were used to build slice-wise nuisance regressors, with a model-based approach derived from the RETROspective Image CORrection (RETROICOR) procedure (Glover et al., 2000). This method assumes the physiological processes to be quasi-periodic, which means that cardiac and respiratory phases can be uniquely assigned for each image. The signals are then modeled using a low-order Fourier expansion subsampled at the time of image acquisition. This technique

has been shown to be efficient for brainstem (Harvey et al., 2008) and spinal cord imaging (Brooks et al., 2008; Kong et al., 2012), where the inclusion of higher order terms was found to be beneficial. Note that 32 regressors are most commonly used to correct for physiological noise in the spinal cord (Kong et al., 2012). Considering the relatively low number of volumes of each run (102 vol), a solution requiring less regressors was favored, so as to limit the number of degrees-of-freedom, while still accounting for respiratory and cardiac terms as well as for the interaction between those processes, which was demonstrated to be a significant source of noise (Brooks et al., 2008). As such, we used the optimized model presented by Harvey et al. (2008) and previously employed in the spinal cord by Tinnermann et al. (2017). Specifically, the physiological noise modelling (PNM) tool from FSL was used to yield 18 voxelwise noise regressors. Finally, the signal from the CSF (mean signal in the 10% of CSF voxels whose signal varies the most) was also included as an additional physiological noise regressor, as recommended by Kong et al. (2012).

2.5.4. Normalization

To allow comparison between the different movements and subjects, a two-step registration procedure was used to register the images to a template space (i.e., PAM50 template, De Leener et al., 2018), using the Spinal Cord Toolbox (De Leener et al., 2017); i) Anatomical-to-template: a binary mask of the spinal cord was automatically created based on the T2-weighted anatomical image. Subsequently, vertebrae were automatically labelled after manual initialization of the C2–C3 vertebral disk. The spinal cord was straightened along its centerline using the anatomical labels and non-rigid registration to the PAM50 template was performed. This step generates an anatomical image warped into the template space, a template image warped into the anatomical space, as well as the corresponding warping fields; ii) Functional-to-anatomical: the functional images were registered to the template in anatomical space with non-rigid transformations, generating the corresponding warping fields. The warping fields from steps i) and ii) were finally concatenated to obtain the functional-to-template transformation. Mean normalized anatomical and functional images are presented in Fig. S2B.

2.5.5. Segmentation

Segmentation of the T2-weighted anatomical image was automatically performed using the Spinal Cord Toolbox (De Leener et al., 2017), generating binary masks of the spinal cord and CSF. As for functional images, binary masks of the spinal cord and CSF were manually drawn.

2.6. fMRI analysis

2.6.1. fMRI-based estimation of spinal activity

FMRI data analysis was carried out using FSL's fMRI Expert Analysis Tool (FEAT). At the subject-level, the preprocessed images of each run (in the native space, after motion correction) were spatially smoothed and highpass temporal filtering (sigma = 45.0 s) was applied. In order to preserve anatomical consistency, spatial smoothing was performed along the centerline of the spinal cord, using a 3D Gaussian kernel with a full width half maximum (FWHM) of $2 \times 2 \times 6\,mm^3$. Using these preprocessed time-series, a first-level statistical analysis (intra-subject – within run) was carried out using FMRIB's Improved Linear Model (FILM) with local autocorrelation correction (Woolrich et al., 2001). The design matrix included the explanatory variables, the physiological noise regressors as well as the outlier volumes for motion scrubbing (see 2.5.2). Specifically, the explanatory variables were defined based on the temporal dynamics of the task (block design), which was convolved with three optimal basis functions using FMRIB's Linear Optimal Basis Set (FLOBS) (Woolrich et al., 2004b), in order to account for differences of hemodynamic response function (HRF) between regions and subjects. The second and third waveforms (i.e., the temporal and dispersion derivatives, respectively) were orthogonalized to the first waveform. For each subject and movement, the parameter estimates corresponding to the first FLOBS waveform (i.e., task against rest), obtained independently for the two runs, were combined by passing them up to a second level analysis (intra-subject – across runs), in which task-specific subject level activation maps were obtained using a fixed-effects model.

Parameter estimates obtained during the second level analyses (i.e., subject-level) were then normalized to the PAM50 template (i.e., functional-to-template transformation) and passed up to a third level analysis (inter-subjects) to obtain average group activation maps using FMRIB's Local Analysis of Mixed Effects (FLAME) stages 1 and 2 with outlier detection (Woolrich et al., 2004a; 2008). Z statistic images were thresholded using clusters determined by $Z > 2$ and a cluster-defining threshold of $p < 0.01$ to account for multiple comparisons. Recent discussions have highlighted concerns regarding the use of parametric testing with a cluster-defining threshold larger than $p = 0.001$ for whole brain fMRI (Eklund et al., 2016). However, our approach is in agreement with recent spinal cord literature (e.g., Tinnermann et al., 2017; Weber et al., 2016a), where the smaller number of voxels curtails the impact of the multiple comparison problem. Furthermore, the use of FSL's FILM to correct for autocorrelation minimizes inflation in the false positive rate (Faull et al., 2015). Besides, we also assessed the presence of false positives using a control analysis (see 2.6.2). Dice coefficients (Dice, 1945) between the individual movement-related activation patterns were also computed (values ranging from 0 – no similarity – to 1 – equal), so as to assess to what extent the thresholded maps were spatially similar for the different movement types.

In order to relate EMG- and fMRI-derived activation maps, the group-level parameter estimates (i.e., beta maps from the third-level analysis) were masked in order to isolate the motor and sensory components of the signal (i.e., the anterior or posterior hemicords) and summed over the x and y dimensions to generate one-dimensional projections along the z dimension. These projections were smoothed (moving average filter, window length of about one spinal level) to summarize the trends of the distributions and compared to the EMG-derived projections using Pearson's correlation coefficients.

2.6.2. Control analysis

In order to evaluate the presence of false positives, an additional control analysis was performed, similarly to Weber et al. (Weber et al., 2016a, 2016b). The preprocessed timeseries of the task-free run recorded at the beginning of the experiment were analyzed following the same procedure as the task runs (i.e., GLM where the explanatory variable was computed using the temporal dynamics – onsets and durations – of an actual task run). Equivalently to the task runs, we computed a group average activation map (thresholded using clusters determined by $Z > 2$ and a cluster-defining threshold of $p < 0.01$). For each subject independently, we also calculated the percentage of spatial extent (number of active voxels divided by the number of voxels in the region of interest; i.e., the C5 to C8 spinal levels) and the average Z-score of the active voxels. This was done in the template space to allow comparison between subjects. Z statistic images were thresholded at $Z > 2$ ($p = 0.01$, uncorrected). In order to compare task-free runs with task runs, we also computed those metrics for all runs of the experiment and averaged results over movement type, independently for each subject. Task-free and task results across subjects were then compared using two-tailed paired t-tests.

2.6.3. Multivoxel pattern analysis

For each subject, MVPA was performed to confirm the task-specific characteristics of the rostrocaudal activations patterns derived using fMRI activity. Images were processed as presented in 2.5. Due to the small number of subjects, group activation maps were obtained using a fixed-effects model. Z statistic images were thresholded using clusters determined by $Z > 2$ and a cluster-defining threshold of $p < 0.001$ to account for multiple comparisons. In order to preserve the information content before deploying MVPA, the dataset was also smoothed using a 3D Gaussian kernel with a full width half maximum (FWHM) of $1 \times 1 \times 3\,mm^3$. Parameter estimates were obtained for each run using the same GLM as presented above (see 2.6.1) but where the explanatory

variables were the task dynamics of the three movements. We defined three contrasts, one for each movement type against rest. The resulting parameter estimates (in the native space) were masked to include the C5 to T1 spinal levels. All voxels were used as inputs (no feature selection) and a three-class LDA classifier similar to the EMG-classifier was employed, with leave-one-run-out cross validation. In order to compare the information content of different regions-of-interest, classification was also performed within specific masks (superior and inferior levels, as well as anterior and posterior hemicords). Confusion matrices were computed considering all cross validation folds, to summarize the accuracy of the classification. Statistical significance was computed following the same procedure as the EMG-based classification (see 2.4.2). Finally, we also assessed the stability of the LDA weight maps, by computing the Pearson's correlation coefficients between the LDA weights of each fold.

3. Results

3.1. Data quality assessment

All subjects completed Phase 1 (EMG experiment) and Phase 2 (fMRI experiment), and 6 of them completed Phase 3 (MVPA experiment). Subjects' performance was monitored during each phase and the quality of the preprocessing steps was visually assessed. As for EMG, data were inspected to rule out the presence of movement artifacts. The assessment of the fMRI data prompted the exclusion of two subjects from further analyses (fMRI and related EMG), as their functional scans did not include the C8 spinal level. A region spanning C5 to C8 spinal levels was imaged in all the remaining subjects (Fig. 3A). In order to assess the impact of the different processing steps, we computed the tSNR on the task-free time-series, by dividing the average signal over time by the standard deviation. The efficiency of the motion correction procedure was confirmed by a significant increase ($p < 0.001$, two-tailed paired *t*-test) of the average tSNR (±SE) from 5.15 ± 0.16 before motion correction to 7.92 ± 0.15 after motion correction (Fig. S2A). The tSNR further increased to 28.22 ± 0.67 ($p < 0.001$) thanks to temporal filtering and spatial smoothing. Overall, the motion of the spinal cord was limited, as highlighted by the average absolute value of the framewise displacement (±SE) ($FD_x = 0.106 \pm 0.002$ mm and $FD_y = 0.143 \pm 0.002$ mm), and only weakly correlated with the task ($\rho_x = 0.063 \pm 0.005$ and $\rho_y = 0.124 \pm 0.004$).

3.2. Rostrocaudal activation patterns captured using EMG and fMRI

3.2.1. EMG-derived spinal maps

In order to estimate task-related spinal activity, we first computed EMG-derived spinal maps. These maps are based on anatomical mapping (Fig. 2A) and they, therefore, represent the theoretical spinal activation patterns. As hypothesized, the spinal activation patterns elicited by the three motor tasks (wrist extension or WE, wrist adduction or WA and finger abduction or FA) exhibited distinct rostrocaudal organizations (Fig. 2B). Notably, the activity shifted from higher cervical segments during wrist extension to lower spinal regions during wrist adduction and finger abduction. Specifically, the activity elicited by wrist extension was relatively spread out and mainly distributed over the C5–C7 spinal levels. This pattern is associated with EMG activity in the wrist extensor muscles as well as in more proximal muscles, such as the brachioradialis (Fig. S3, Table S1). For the wrist adduction, instead, the activity was mainly focused in C7 and C8, coinciding with EMG activity in the flexor and extensor carpi ulnaris. Finally, finger abduction presented an activation pattern similar to the one of wrist adduction, but with an activity peak more focalized over C8, explained by EMG activity in the finger extensor muscles, as well as in distal muscles such as the abductor digiti minimi (Fig. S3).

We evaluated the stability of the rostrocaudal patterns over repetitions (Fig. 2C), which highlighted more variability for the maps related to wrist extension ($r = 0.78 \pm 0.07$, mean over subjects ± SE) compared to the patterns of wrist adduction ($r = 0.92 \pm 0.04$) and finger abduction ($r = 0.97 \pm 0.01$).

This characterization of the estimated spinal activity confirmed that the selected movements required distinct rostrocaudal cervical activations, and they were, thus, apt to explore the potential of fMRI in capturing the complexity of human spinal cord functional activity.

3.2.2. fMRI-derived spinal maps

In order to elucidate whether spinal cord BOLD activity also displayed a similar task-specific rostrocaudal organization, we computed fMRI-derived spinal maps. After preprocessing, we assessed group level spinal activity using a GLM with mixed-effects modelling. For all movements, a larger portion of the active voxels was observed in the anterior (i.e., motor) part of the spinal cord ($56.44 \pm 2\%$, mean over movements ± SD, see sagittal slices in Fig. S4), while the activity was roughly distributed evenly between left and right hemicords ($47.65 \pm 17.8\%$ in the right hemicord), as expected for bimanual motor tasks. Activity was also spread out between the grey and white matter ($33.84 \pm 8.5\%$ in the grey matter), in accordance with reports from Weber and colleagues (Weber et al., 2017). Similarly to the EMG-derived spinal maps, wrist extension resulted in more rostral activity than wrist adduction and finger abduction (Fig. 3B and C, Table S2). Specifically, the activity related to wrist extension was mainly located in the C6 spinal level

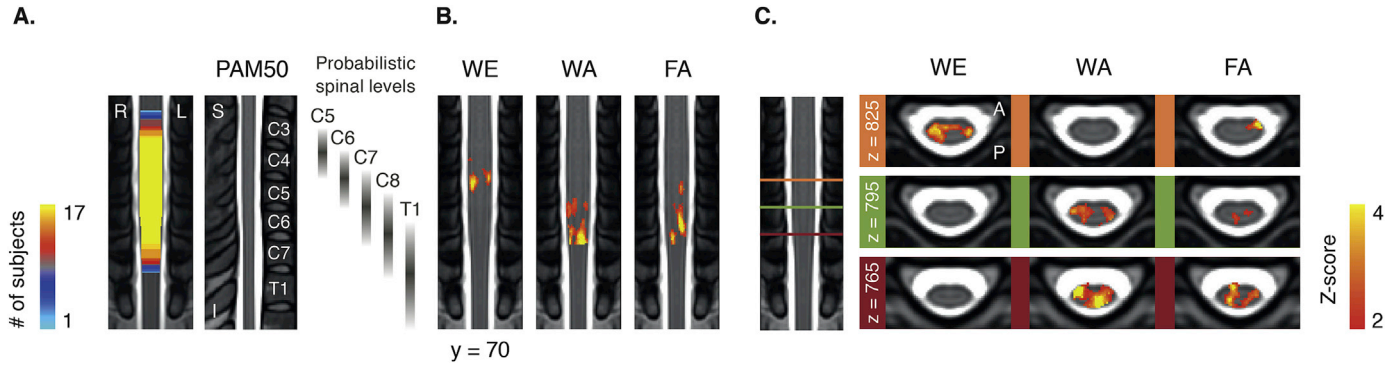

Fig. 3. | **Characterization of rostrocaudal spinal activation patterns (fMRI)** | **A.** Imaged regions map, normalized to the PAM50 template (De Leener et al., 2018). The color bar indicates the number of subjects with the corresponding region included in the functional maps. A sagittal view of the PAM50 template is presented for reference. The vertebral bodies are labelled, as well as the corresponding probabilistic spinal levels (Cadotte et al., 2015). **B.** Group activation maps (mixed-effects modelling) for the contrast task VS baseline (WE = wrist extension, WA = wrist adduction, FA = finger abduction). Maps are thresholded at a Z-score > 2 (cluster-defining threshold of $p < 0.01$) and normalized to the PAM50 template. Only a region from C5 to C8 is considered (imaged in all subjects). Central coronal views are presented, with the same slice (y = 70) shown for all movements. **C.** Three axial slices (z = 765, z = 795 and z = 825, see left panel) are presented (right panel), overlaid on the PAM50 template. For sagittal slices, see Fig. S4. S = superior, I = inferior, L = left, R = right, A = anterior, P = posterior.

(81.8% of the active voxels), while it was also the only movement eliciting activity in the C5 spinal level (12.9% of the active voxels). The main activity peak during wrist adduction and finger abduction, instead, was focused in C8 (respectively 68.7% and 55.4% of the active voxels), while the remaining activations were only found in the C7 spinal level. The difference between these activation patterns was also illustrated by the low Dice coefficients between them ($D = 0$ between WE and WA, $D = 0.04$ between WE and FA and $D = 0.36$ between WA and FA).

These results highlight that the BOLD activity reveals a distinct rostrocaudal cervical organization associated with different upper limb movements, consistent with the one inferred using anatomy-based mapping.

3.2.3. The activation patterns are specific to task runs

In order to control for false positives, we employed a control analysis in which the same procedure as the one used to detect task-related activity was applied to task-free runs. At the group level, no voxel exceeded the significance threshold when combining the task-free activation maps from all subjects (Fig. 4A), emphasizing that task-free activity was not localized in a particular spinal level.

We then further assessed the significance of fMRI activation during task runs by comparing both the extent and amplitude of the activity linked to task and task-free runs at the subject-level, similarly to Weber et al. (Weber et al., 2016b, 2016a). The spatial extent of the activity (i.e., percentage of activated spinal cord) identified during the task runs (Figs. 4B and $8.44 \pm 1.16\%$, mean over subjects $\pm$ SE) was significantly larger ($p < 0.001$) than during the task-free runs ($2.97 \pm 0.47\%$). Similarly, the intensity of the activity, as illustrated by the average Z-score over the active voxels, was significantly higher ($p < 0.01$) during the task runs (Figs. 4B and 2.56 ± 0.04) than during the task-free runs (2.38 ± 0.03).

These combined results indicate that the cervical rostrocaudal activation patterns imaged during task runs are likely not artefactual and reflect motoneuron activity.

3.2.4. EMG- and fMRI-derived spinal maps present similar rostrocaudal distributions

To further examine the similarities between the rostrocaudal distributions of spinal activity extracted using EMG and fMRI and, thus, to confirm the specificity of spinal BOLD signal, we compared the obtained activation patterns using their respective projections along the z direction. When focusing on the anterior (i.e., motor) profiles (Fig. 5), similar distributions were observed for both modalities, with task-related profiles shifted towards rostral or caudal spinal levels, depending on the motor task. During wrist extension, the spread of activity was stronger at the rostral part of the cord, while the activity during wrist adduction and finger abduction was more localized in the caudal region. The projections of activity derived from the two modalities were significantly correlated ($p < 0.001$), as stressed by the correlation coefficients ρ between the EMG- and fMRI-derived trends: 0.32 for wrist extension, 0.90 for wrist adduction, and 0.70 for finger abduction. These moderate to high correlations indicate similar rostrocaudal distributions, inferred either peripherally from the EMG activity or directly from functional imaging of the spinal activity, and it supports the use of fMRI to directly image spinal cord involvement during upper limb movements. In addition, the profiles of WA and FA, both shifted towards the caudal side of the cord, also exhibited a high correlation between their related EMG- and fMRI-derived profiles (e.g., $\rho = 0.96$ between the fMRI-derived profile of WA and the EMG-derived profile of FA, see full correlation matrix in Fig. S5A). This is, however, in accordance with the high correlation of 0.98 between the EMG-derived profiles of those two movement types (see Fig. S5C). Interestingly, the fMRI-derived projections, when considering only the posterior (i.e., sensory) component of the spinal activity, were also highly correlated ($p < 0.001$) with the EMG-derived projections ($\rho_{WE} = 0.73$, $\rho_{WA} = 0.87$ and $\rho_{FA} = 0.43$) (Fig. S5B).

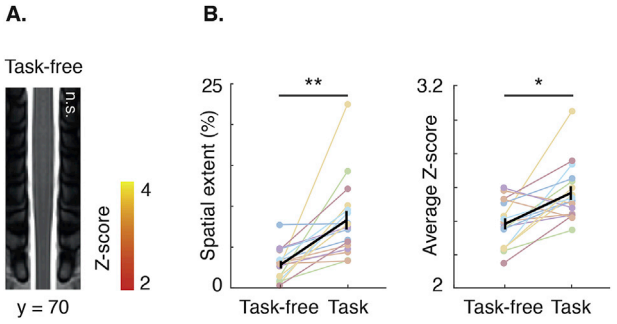

Fig. 4. | **Control analyses** | **A.** Group activation maps (mixed-effects modelling) for the control analysis (task-free runs). Maps are thresholded at a Z-score > 2 (cluster-defining threshold of $p < 0.01$) and normalized to the PAM50 template (coronal view). n.s. indicates that no significant activity was detected. **B.** Comparison of the percentage spatial extent of the activity, relative to the C5 to C8 region of the spinal cord (left panel), and average Z-score (right panel) during the task-free and task runs. Each colored line corresponds to one subject. The black line corresponds to the mean ± SE. * corresponds to $p < 0.01$ and ** to $p < 0.001$ (two-tailed paired *t*-test).

3.3. Imaged rostrocaudal organization is task-specific

Both EMG- and fMRI-derived spinal maps suggest task-specific rostrocaudal distributions of the cervical spinal cord activity. In order to verify this hypothesis, we used a machine learning approach that exploits the information content of each motor task in the spinal maps derived from both modalities.

When using EMG-derived projections (i.e., time-averaged) of the estimated spinal activity as features (i.e., one feature for each spinal level), the classifier was able to differentiate the three classes with a high accuracy, as emphasized by the diagonal confusion matrix (Fig. 6A). The overall accuracy (95%) was significantly higher than chance ($p < 0.01$, permutation testing, chance level at ~33%), highlighting the specificity of the estimated spinal activation patterns.

Furthermore, we deployed MVPA to decode the executed task based on the voxelwise spinal BOLD activity. When using information from the whole spinal cord, rostrocaudal activation patterns allowed to decode movements for all three classes with an overall accuracy of 54.5% (Fig. 6B), significantly better than chance ($p < 0.01$). The stability of the LDA weight maps over cross-validation folds was also assessed by computing their average Pearson's correlation coefficients. This analysis showed a high correlation between folds (0.87 ± 0.01, mean over subjects ± SE).

In order to investigate the relative contribution of different subregions of the cord, we performed the classification independently: i) for inferior and superior spinal levels and ii) for each hemicord (i.e., anterior and posterior) (Fig. S6). Although wrist adduction and finger abduction could still be decoded using both rostral and caudal segments, wrist extension failed to be detected using the inferior region of the cord (38.4%), emphasizing the rostral character of the related activation. Interestingly, movements could be classified efficiently using both anterior and posterior hemicords (average classifications of 48,4% and 51.1%, respectively), highlighting the shared influence of motor and sensory processes.

Finally, to validate the rostrocaudal cervical patterns presented in 3.2.2, we assessed the group level activity elicited by the three movements during the MVPA experiment (Fig. 6C, Table S3). This analysis uncovered activation maps consistent with those imaged during the first experimental session (Fig. 3B). Similarly, the three different task-related patterns presented distinct spatial distributions ($D = 0.33$ between WE and WA, $D = 0.15$ between WE and FA and $D = 0.19$ between WA and FA). More specifically, activation patterns related to wrist extension were located in higher spinal levels (8.3% of the active voxels in C6, and 65.4% in C7) than the ones elicited by wrist adduction (45.1% in C7, 29.4% in

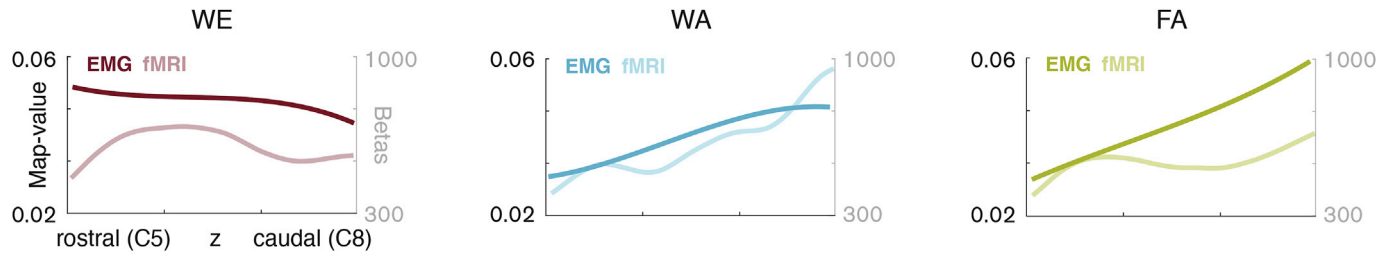

Fig. 5. | **Rostrocaudal distributions of activations** | For each movement type (WE = wrist extension, WA = wrist adduction, FA = finger abduction), distributions of the EMG- (dark line) and fMRI- (light line) derived spinal maps along the *z* direction are presented. Time-averaged-map values are used for the projections of EMG-derived spinal map while group parameter estimates (anterior, or motor, hemicord), summed over the *x* and *y* dimensions, are used for the projection of fMRI-derived spinal maps. Spinal levels are displayed on the *x*-axis, and *y*-axis corresponds to the projected map-values (EMG) or betas (fMRI). Pearson's correlation coefficients between the two modalities are respectively 0.32 ($p < 0.001$), 0.90 ($p < 0.001$) and 0.70 ($p < 0.001$).

C8 and 23.4% in T1) or finger abduction (50% in C8 and 50% in T1). These results further demonstrate the robustness of the task-specific rostrocaudal organization.

These combined results corroborate the hypothesis that the measured BOLD signal actually reflects the spinal processes underlying movement. They, therefore, support the potential of fMRI to image task-specific rostrocaudal organization, offering as such the prospect of a novel tool to study spinal function and its disruption in neurological conditions.

4. Discussion

Here, we hypothesized that spinal cord fMRI could be used to reliably image task-specific activity in different cervical segments during distinct upper limb movements. To address this question, we combined spinal functional imaging with EMG recordings, as advised in previous studies (Madi et al., 2001; Weber et al., 2016b). Specifically, we exploited anatomical knowledge of muscle innervation to infer the contribution of each muscle to the spinal activity in the different segments. Notwithstanding the limitations inherent to the imaging of spinal cord function, we acquired distinct task-specific rostrocaudal activation patterns using fMRI, consistent with the theoretical maps derived from the muscular recordings. These task-specific spinal maps allowed for a successful decoding of motor tasks. Here we discuss our results with an emphasis on acquisition and processing precautions for reliable spinal fMRI BOLD signal.

4.1. Imaged cervical activation patterns have a task-specific rostrocaudal organization

To characterize the specificity of the activation in the rostrocaudal direction, we selected movements that allowed capitalizing on the different locations of the motoneuron pools innervating the employed muscles. Wrist extension, if performed with no radial or ulnar deviation, should mainly be linked to motoneuron activity in the C6–C7 spinal levels, while wrist adduction and finger abduction were expected to elicit lower activity, in the C7–C8 and C8-T1 segments, respectively (Table S1). These task-specific rostrocaudal activations were first confirmed using EMG recordings (Fig. 2). Muscular activity was mapped back onto the spinal cord using anatomical knowledge of muscle innervation. As expected, the activity shifted from rostral levels for wrist extension to caudal regions for wrist adduction and finger abduction. However, these maps, derived from indirect peripheral recordings, are solely based on anatomical considerations and, thus, do not fully inform on the actual spinal cord function. Conversely, fMRI enables localized observation of spinal cord activity. Using this technique, we showed that spinal BOLD signal also reflected these task-specific activations patterns (Fig. 3). In line with the findings of Madi et al. (2001), we observed higher activations for wrist extension than for finger abduction. Nonetheless, the detected activity was more focal in our study, possibly due to the increased field strength, the choice of sequence (selective field-of-view imaging), and to the ad hoc noise correction steps applied to the signal. Wrist adduction, which was not performed in the study of Madi

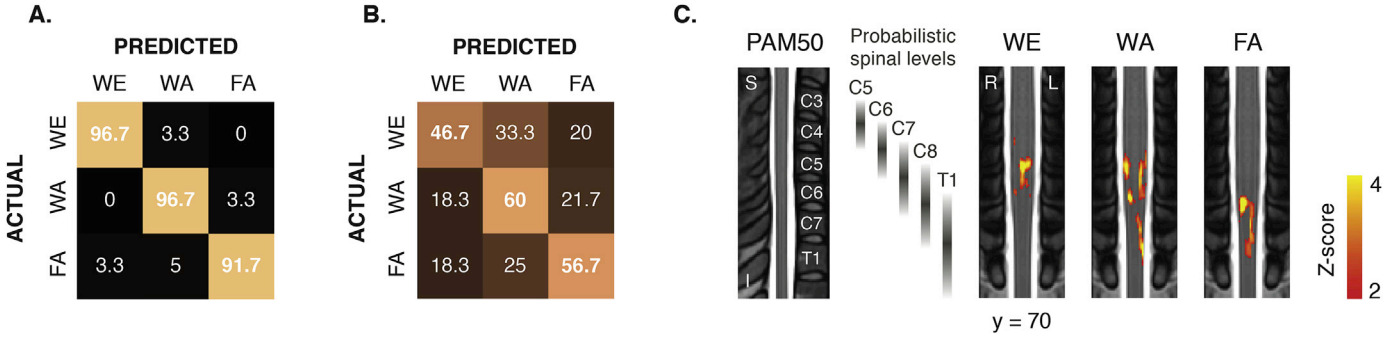

Fig. 6. | **Average decoding accuracy** | **A.** Each subject performed 10 repetitions of each movement. EMG-derived spinal maps were computed for each repetition and averaged over time to keep only the spatial information (i.e., five features per sample, corresponding to the mean activity over time in the spinal levels from C5 to T1). Classification was performed in each subject using an LDA classifier (leave-one-movement-out cross validation). Confusion matrices were then averaged over subjects (here, only the six subjects who participated in the MVPA experiment were considered). The average accuracy over subjects and conditions was 95% and significantly above the chance level ($p < 0.01$, permutation testing, chance level at ~33%). All values are reported in percentage. **B.** Multivoxel pattern analysis (MVPA) was performed in each subject, using data from the C5 to T1 spinal levels and a LDA classifier (leave-one-run-out cross validation). Confusion matrices were averaged over subjects. The average accuracy over subjects and conditions was 54.5% and significantly above the chance level ($p < 0.01$, permutation testing). **C.** Group activation maps (of the six subjects who participated in the MVPA experiment) for the contrast task VS baseline. Maps represent the mean activity over the group (fixed-effects analysis) and are thresholded at a Z-score > 2 (cluster-defining threshold of $p < 0.001$). All maps are normalized to the PAM50 template (De Leener et al., 2018). Coronal views are presented, with the same slice shown for all movements. A sagittal view of the PAM50 template is shown as a reference, with the corresponding probabilistic spinal level. WE = wrist extension, WA = wrist adduction, FA = finger abduction. S = superior, I = inferior, L = left, R = right.

et al., also elicited the expected activity, with an activation profile shifted towards caudal segments. For the three movements, the activity was equally distributed between the left and right hemicords and mainly located in the anterior (i.e., ventral) hemicord. This is in agreement with anatomical knowledge, as movements were performed bilaterally and motoneurons are found in the ventral horns. Despite the larger anterior activity, significant activity was also found in the posterior (i.e., dorsal) hemicord. As the task consisted in performing dynamic repetitions of the movements, this is likely resulting from sensory processes and proprioception. In parallel, a control analysis where we applied our analysis pipeline to task-free runs emphasized that the imaged cervical patterns were likely not of artefactual origin (Fig. 4).

In a subsequent step, we quantified the relationship between the EMG- and fMRI-derived spinal maps by using their respective projections on the z dimension (i.e., spinal levels) and demonstrated analogous rostrocaudal distributions of activity between the two modalities (Fig. 5). This suggests that both activation maps stem from the same motor-related spinal processes, hence supporting the use of fMRI to reliably and directly image task-related rostrocaudal cervical activity.

In order to further confirm the identified task-specific activation patterns, we employed a machine learning paradigm on a subset of participants, so as to decode motor tasks based on spinal activation maps. FMRI-derived patterns presented significant decoding performances (54.5%), highlighting the task-specific information contained in the acquired BOLD signal. Wrist extension, however, presented a lower classification accuracy (46.7%), potentially related to higher movement variability when executing this task. This hypothesis is supported by the theoretical EMG-derived spinal maps, where a lower correlation was observed between the activation patterns of the different repetitions of this movement (Fig. 2), possibly indicating that the wrist was not consistently moved in the expected neutral ulnoradial deviation. Nevertheless, it should be emphasized that wrist extension and adduction, although involving the same joint, could be distinguished with a significant accuracy. Interestingly, when using only the inferior portion of the spinal cord, wrist extension tended to be mistaken for wrist adduction (Fig. S6A), further supporting the rostral character of the underlying activation.

Another compelling finding concerned the high decoding performances obtained when using the anterior or posterior hemicord only (48.4% and 51.1%, respectively, see Figs. S6C–D). This suggests that both motor and sensory processes were reliably captured by spinal cord fMRI and were both task-specific. The task-specificity of sensory information parallels recent findings from Yeganegi et al. (2018). In that study, the authors showed for the first time that electrophysiological recordings of dorsal grey matter activity in anesthetized cats allowed for successful decoding of hind limb movements. Indeed, movements not only elicit efferent signals travelling from the ventral horns of the spinal cord to the muscles, they also involve afferent feedback provided by sensory receptors (e.g., muscles spindles, tendons or mechanoreceptors) and going to the central nervous system, through the dorsal horns of the spinal cord (Enoka, 2008). Consequently, observing task-specific sensory activity is not unexpected, as also reflected by the significant correlations obtained between the EMG- and fMRI-derived profiles, when considering the sensory component only (see 3.2.4).

Importantly, the group activation maps resulting from this additional imaging session presented similar rostrocaudal patterns as the ones derived from the initial experiment, confirming the robustness of the captured rostrocaudal activation patterns. Altogether, these results underscore the broad potential of spinal cord fMRI, not only to image spinal motoneuron activity, but also to explore sensory and proprioceptive mechanisms, one aspect that cannot be probed with peripheral recordings, such as EMG acquisitions. To our knowledge, our study is the first report of MVPA in the spinal cord during different types of movements (note, however, that Weber and colleagues previously used MVPA to decode left and right wrist flexions (Weber et al., 2016b)).

4.2. Methodological challenges of spinal cord fMRI and possible solutions

Although spinal cord fMRI relies on the same principles as brain fMRI, it presents additional challenges (Giove et al., 2004) and has therefore not yet received as much interest. First, the small cross-sectional dimensions of the spinal cord prompt the need for high resolution imaging to avoid partial volume effects and to unravel the details of the structure of interest. Second, the spinal cord is surrounded by different tissue types, whose disparate magnetic susceptibilities affect the static magnetic field. This can lead to image artifacts, such as distortions or signal dropouts, when standard T2*-weighted fMRI protocols are employed. Advancements in terms of hardware (Cohen-Adad et al., 2011) and sequences (Finsterbusch et al., 2012) are currently being proposed in order to obviate these constraints. Finally, another prominent issue is related to the close proximity of the lungs, the heart and other visceral organs, which are important sources of motion (Piché et al., 2009). Notably, cardiac activity generates a pulsatile flow in the cerebrospinal fluid (CSF) around the spinal cord.

In our study, we employed different approaches, from data acquisition to (pre-)processing, to overcome these limitations and get a reliable signal. Specifically, prior to acquisition, shimming adjustments focused on the cervical spinal cord were carried out to optimize the field homogeneity in the region of interest. The acquisition was performed using selective field-of-view imaging, hence increasing imaging speed while allowing for high spatial resolution ($1 \times 1 \times 3$ mm). In order to curtail the detrimental effect of motion, we applied several processing steps. Realignment was first conducted using a slice-wise procedure, accounting for the articulated structure of the spinal cord (Cohen-Adad et al., 2009; De Leener et al., 2017). Outlier volumes were then identified and included as confounds during the GLM analysis. Finally, we used the physiological recordings acquired throughout the experiment to model additional nuisance regressors, based on the RETROICOR procedure (Glover et al., 2000), and a CSF regressor was also included. Both approaches have been demonstrated to improve activation statistics (Brooks et al., 2008), and their impact was reflected by the increase in tSNR observed consecutive to these processing steps (see 3.1 and Fig. S2). In addition, the GLM analysis was also adapted to account for potential variations of the HRF, compared to the canonical HRF commonly employed. Indeed, the temporal properties of the spinal HRF are still unclear (Giulietti et al., 2008) and no solution to tackle this limitation has so far been proposed in the context of spinal cord fMRI. Therefore, we opted for an approach previously used in brainstem fMRI (e.g., Faull et al., 2015), a field facing similar challenges in this regard (Devonshire et al., 2012) and employed a FLOBS-generated basis set instead of the canonical HRF (Woolrich et al., 2004b), so as to be less sensitive to hemodynamic variability (e.g., dispersion, delay or shape).

Following this advanced pipeline, we were able to image robust rostrocaudal patterns. Nevertheless, some limitations need to be acknowledged. Regardless of the consistent sequence of motoneuron pools across subjects (e.g., distal arm muscles innervated by lower spinal levels than proximal muscles), individual differences in the location of spinal levels with respect to the corresponding vertebral bodies have previously been reported (Cadotte et al., 2015). When registering subject data to a common template, these differences are not taken into account with current normalization algorithms, an issue which was already raised by Weber et al. (2016a, 2016b). This could hinder our ability to detect activation patterns along the rostrocaudal direction, due to potential mismatches between subjects. Although less prevalent, similar issues exist in brain fMRI (Dubois and Adolphs, 2016) and progresses in both fields (e.g., advanced algorithms or functionally-informed alignment) could gradually overcome these difficulties.

4.3. Experimental limitations and considerations

Our paper aimed to relate EMG and fMRI activity in order to highlight the neural origin of the signal recorded with spinal cord fMRI. This

represents a first step in showing that this technique can shed light on spinal motor responses. We believe that future studies could deploy similar motor-based paradigms, to infer general principles regarding human spinal cord functional organization. We propose hereafter a number of experimental and technical recommendations. While the structure of our experiment (i.e., two complementary sessions to record EMG and fMRI) imposed certain timing constraints to prevent subjects' fatigue, future studies focusing solely on fMRI recordings could potentially limit the number of conditions, so as to increase the scan duration, or the number of runs, to further explore the properties of the underlying spinal signals. An additional aspect that may be of interest is the variability of movement execution. Indeed, as muscle activations were not performed at a specific percentage of the Maximum Voluntary Contraction, the exact output of the muscles during the fMRI scans was not controlled. Performing isometric tasks could help in this regard, although it may require the use of custom splints, which need to be adapted to the movements of interest. Finally, we recommend the use of a soft cervical collar for the functional recordings, as this helps stabilize and straighten the neck, hence participating to improve image quality.

4.4. Conclusion

Despite technological challenges, we captured variations in spinal activity and revealed task-specific rostrocaudal patterns in agreement with the anatomical arrangement of motoneuron pools. These results contribute to advance our understanding of the potential of spinal cord fMRI. They demonstrate its prospects as a reliable tool to investigate spinal cord function and to further understand mechanisms involved in motor control and neurological motor disorders, such as spinal cord injury or multiple sclerosis. For instance, spinal cord fMRI could allow exploiting information on spinal sensorimotor function, rather than theoretical estimations such as EMG-based maps. Eventually, we foresee that such advances in our knowledge of the spinal cord could support clinical decision-process and help inform intervention procedures.

Declarations of interest

None.

Acknowledgements

The authors would like to thank all the volunteers enrolled in the study. We thank Dr. Camilla Pierella and Dr. Marco Capogrosso for their comments on the article, and Thomas Bolton for his thoughtful suggestions. This study was partly funded by the Wyss Center for Bio and Neuroengineering and the Bertarelli Foundation. This work was supported by the Fondation Campus Biotech Geneva (FCBG), a foundation of the École Polytechnique Fédérale de Lausanne (EPFL), the University of Geneva (UniGE), and the canton of Geneva.

Appendix A. Supplementary data

Supplementary data to this article can be found online at https://doi.org/10.1016/j.neuroimage.2019.05.036.

References

Alstermark, B., Isa, T., 2012. Circuits for skilled reaching and grasping. Annu. Rev. Neurosci. 35 (1), 559–578. https://doi.org/10.1146/annurev-neuro-062111-150527.

Backes, W.H., Mess, W.H., Wilmink, J.T., 2001. Functional MR imaging of the cervical spinal cord by use of median nerve stimulation and fist clenching. Am. J. Neuroradiol. 22 (December), 1854–1859.

Bouwman, C.J.C., Wilmink, J.T., Mess, W.H., Backes, W.H., 2008. Spinal cord functional MRI at 3 T: gradient echo echo-planar imaging versus turbo spin echo. Neuro*image* 43 (2), 288–296. https://doi.org/10.1016/j.neuroimage.2008.07.024.

Brooks, J.C.W., Beckmann, C.F., Miller, K.L., Wise, R.G., Porro, C.A., Tracey, I., Jenkinson, M., 2008. Physiological noise modelling for spinal functional magnetic resonance imaging studies. Neuroimage 39, 680–692. https://doi.org/10.1016/j.neuroimage.2007.09.018.

Cadotte, D.W., Cadotte, A., Cohen-Adad, J., Fleet, D., Livne, M., Wilson, J.R., Mikulis, D., Nugaeva, N., Fehlings, M.G., 2015. Characterizing the location of spinal and vertebral levels in the human cervical spinal cord. Am. J. Neuroradiol. 36 (4), 803–810. https://doi.org/10.3174/ajnr.A4192.

Cappellini, G., Ivanenko, Y.P., Dominici, N., Poppele, R.E., Lacquaniti, F., 2010. Migration of motor pool activity in the spinal cord reflects body mechanics in human locomotion. J. Neurophysiol. 104 (6), 3064–3073.

Cohen-Adad, J., Rossignol, S., Hoge, R.D., 2009. Slice-by-slice motion correction in spinal cord fMRI: SliceCorr. In: Proceedings of the 17th Annual Meeting of the International Society for Magnetic Resonance in Medicine. Honolulu, USA.

Cohen-Adad, J., Mareyam, A., Keil, B., Polimeni, J.R., Wald, L.L., 2011. 32-Channel RF coil optimized for brain and cervical spinal cord at 3 T. Magn. Reson. Med. 66 (4), 1198–1208.

Coscia, M., Monaco, V., Martelloni, C., Rossi, B., Chisari, C., Micera, S., 2015. Muscle synergies and spinal maps are sensitive to the asymmetry induced by a unilateral stroke. J. NeuroEng. Rehabil. 12 (39) https://doi.org/10.1186/s12984-015-0031-7.

Coutanche, M.N., Thompson-Schill, S.L., 2012. The advantage of brief fMRI acquisition runs for multi-voxel pattern detection across runs. Neuroimage 61 (4), 1113–1119. https://doi.org/10.1016/j.neuroimage.2012.03.076.

Devonshire, I.M., Papadakis, N.G., Port, M., Berwick, J., Kennerley, A.J., Mayhew, J.E.W., Overton, P.G., 2012. Neurovascular Coupling Is Brain Region-dependent, vol 59. Elsevier Inc., NeuroImage, pp. 1997–2006. https://doi.org/10.1016/j.neuroimage.2011.09.050, 3.

Dice, L.R., 1945. Measures of the amount of ecologic association between species. Ecology 26 (3), 297–302. https://doi.org/10.2307/1932409.

Dubois, J., Adolphs, R., 2016. Building a science of individual differences from fMRI. Trends Cognit. Sci. 20 (6), 425–443. https://doi.org/10.1016/j.tics.2016.03.014.

Eippert, F., Kong, Y., Jenkinson, M., Tracey, I., Brooks, J.C.W., 2017. Denoising spinal cord fMRI data: approaches to acquisition and analysis. Neuroimage 154, 255–266. https://doi.org/10.1016/j.neuroimage.2016.09.065.

Eklund, A., Nichols, T.E., Knutsson, H., 2016. Cluster failure: why fMRI inferences for spatial extent have inflated false-positive rates. Proc. Natl. Acad. Sci. U.S.A. 113 (28), 7900–7905. https://doi.org/10.1073/pnas.1602413113.

Enoka, R.M., 2008. Neuromechanics of human movement. Human Kinetics, 4 edition.

Faull, O.K., Jenkinson, M., Clare, S., Pattinson, K.T.S., 2015. Functional subdivision of the human periaqueductal grey in respiratory control using 7tesla fMRI. Neuroimage 113, 356–364. https://doi.org/10.1016/j.neuroimage.2015.02.026.

Finsterbusch, J., 2013. Functional neuroimaging of inner fields-of-view with 2D-selective RF excitations. Magn. Reson. Imag. 31 (7), 1228–1235. https://doi.org/10.1016/j.mri.2013.03.005.

Finsterbusch, J., Eippert, F., Büchel, C., 2012. Single, slice-specific z-shim gradient pulses improve T2*-weighted imaging of the spinal cord. In: NeuroImage, vol 59. Elsevier Inc., pp. 2307–2315. https://doi.org/10.1016/j.neuroimage.2011.09.038, 3.

Giove, F., Garreffa, G., Giulietti, G., Mangia, S., Colonnese, C., Maraviglia, B., 2004. Issues about the fMRI of the human spinal cord. Magn. Reson. Imag. 22 (10), 1505–1516. https://doi.org/10.1016/j.mri.2004.10.015.

Giszter, S., Hart, C., Udoekwere, U., 2012. 'The Role of Spinal Cord in Motor Control : reflexes, patterning and final motor production'. ACNR 12 (1), 25–29.

Giulietti, G., Giove, F., Garreffa, G., Colonnese, C., Mangia, S., Maraviglia, B., 2008. Characterization of the functional response in the human spinal cord: impulse-response function and linearity. Neuro*image* 42 (2), 626–634. https://doi.org/10.1016/j.neuroimage.2008.05.006.

Glover, G.H., Li, T.Q., Ress, D., 2000. Image-based method for retrospective correction of physiological motion effects in fMRI: RETROICOR. Magn. Reson. Med. 44 (1), 162–167.

Govers, N., Béghin, J., Van Goethem, J.W.M., Michiels, J., Hauwe, L., Vandervliet, E., Parizel, P.M., 2007. Functional MRI of the cervical spinal cord on 1.5 T with fingertapping: to what extent is it feasible? Neuroradiology 49 (1), 73–81. https://doi.org/10.1007/s00234-006-0162-4.

Grasso, R., Ivanenko, Y.P., Zago, M., Molinari, M., Scivoletto, G., Castellano, V., Macellari, V., Lacquaniti, F., 2004. Distributed plasticity of locomotor pattern generators in spinal cord injured patients. Brain*: J. Neurol.* 127 (Pt 5), 1019–1034. https://doi.org/10.1093/brain/awh115.

Harvey, A.K., Pattinson, K.T.S., Brooks, J.C.W., Mayhew, S.D., Jenkinson, M., Wise, R.G., 2008. Brainstem functional magnetic resonance imaging: disentangling signal from physiological noise. J. Magn. Reson. Imaging 28 (6), 1337–1344. https://doi.org/10.1002/jmri.21623.

Ivanenko, Y.P., Dominici, N., Cappellini, G., Di Paolo, A., Giannini, C., Poppele, R.E., Lacquaniti, F., 2013. Changes in the spinal segmental motor output for stepping during development from infant to adult. J. Neurosci. 33 (7), 3025–3036. https://doi.org/10.1523/JNEUROSCI.2722-12.2013.

Ivanenko, Y.P., Poppele, R.E., Lacquaniti, F., 2006. Spinal cord maps of spatiotemporal alpha-motoneuron activation in humans walking at different speeds. J. Neurophysiol. 95, 602–618. https://doi.org/10.1152/jn.00767.2005.

Jenkinson, M., Bannister, P., Brady, M., Smith, S., 2002. Improved optimization for the robust and accurate linear registration and motion correction of brain images improved optimization for the robust and accurate linear registration and motion correction of brain images. Neuroimage 17 (2), 825–841. https://doi.org/10.1006/nimg.2002.1132.

Jenkinson, M., Beckmann, C.F., Behrens, T.E.J., Woolrich, M.W., Smith, S.M., 2012. 'FSL', Neuroimage 62 (2), 782–790. https://doi.org/10.1016/j.neuroimage.2011.09.015.

Kendall, F.P., McCreary, E.K., Provance, P.G., Rodgers, M.M., Romani, W.A., 2005. Muscles: Testing and Function with Posture and Pain, fifth ed. Lippincott Williams & Wilkins.

Kong, Y., Jenkinson, M., Andersson, J., Tracey, I., Brooks, J.C.W., 2012. Assessment of Physiological Noise Modelling Methods for Functional Imaging of the Spinal Cord. In: NeuroImage, vol 60. Elsevier Inc., pp. 1538–1549, 2.

Kornelsen, J., Mackey, S., 2010. Potential clinical applications for spinal functional MRI. Curr. Pain Headache Rep. 11 (3), 165–170.

Kornelsen, J., Stroman, P.W., 2004. fMRI of the lumbar spinal cord during a lower limb motor task. Magn. Reson. Med. 52, 411–414. https://doi.org/10.1002/mrm.20157.

Kornelsen, J., Stroman, P.W., 2007. Detection of the neuronal activity occurring caudal to the site of spinal cord injury that is elicited during lower limb movement tasks. Spinal *Cord* 45 (7), 485–490. https://doi.org/10.1038/sj.sc.3102019.

De Leener, B., Fonov, V.S., Collins, D.L., Callot, V., Stikov, N., Cohen-Adad, J., 2018. PAM50: unbiased multimodal template of the brainstem and spinal cord aligned with the ICBM152 space. Neuroimage 165, 170–179. https://doi.org/10.1016/j.neuroimage.2017.10.041.

De Leener, B., Lévy, S., Dupont, S.M., Fonov, V.S., Stikov, N., Louis Collins, D., Callot, V., Cohen-Adad, J., 2017. SCT: spinal cord toolbox, an open-source software for processing spinal cord MRI data. NeuroImage 145 (Pt A), 24–43. https://doi.org/10.1016/j.neuroimage.2016.10.009. Elsevier.

Madi, S., Flanders, A.E., Vinitski, S., Herbison, G.J., Nissanov, J., 2001. Functional MR imaging of the human cervical spinal cord. AJNR (Am. J. Neuroradiol.) 22 (9), 1768–1774.

Maieron, M., Iannetti, G.D., Bodurka, J., Tracey, I., Bandettini, P.A., Porro, C.A., 2007. Functional responses in the human spinal cord during willed motor actions: evidence for side- and rate-dependent activity. J. Neurosci. 27 (15), 4182–4190. https://doi.org/10.1523/JNEUROSCI.3910-06.2007.

Marieb, E.N., Hoehn, K.N., 2014. Human Anatomy & Physiology, ninth ed. Pearson.

Ng, M.C., Wu, E.X., Lau, H.F., Hu, Y., Lam, E.Y., Luk, K.D., 2008. Cervical spinal cord BOLD fMRI study: modulation of functional activation by dexterity of dominant and non-dominant hands. Neuroimage 39 (2), 825–831. https://doi.org/10.1016/j.neuroimage.2007.09.026.

Pereira, F., Mitchell, T., Botvinick, M., 2009. Machine learning classifiers and fMRI: a tutorial overview. Neuroi*mage* 45 (1), S199–S209. https://doi.org/10.1016/j.neuroimage.2008.11.007.

Piché, M., Cohen-Adad, J., Nejad, M.K., Perlbarg, V., Xie, G., Beaudoin, G., Benali, H., Rainville, P., 2009. Characterization of cardiac-related noise in fMRI of the cervical spinal cord. In: Magnetic Resonance Imaging, vol 27. Elsevier Inc., pp. 300–310. https://doi.org/10.1016/j.mri.2008.07.019, 3.

Pirondini, E., Coscia, M., Marcheschi, S., Roas, G., Salsedo, F., Frisoli, A., Bergamasco, M., Micera, S., 2016. 'Evaluation of the effects of the Arm Light Exoskeleton on movement execution and muscle activities: a pilot study on healthy subjects.', *Journal of neuroengineering and rehabilitation*. J. NeuroEng. Rehabil. 13, 9. https://doi.org/10.1186/s12984-016-0117-x.

Power, J.D., Mitra, A., Laumann, T.O., Snyder, A.Z., Schlaggar, B.L., Petersen, S.E., 2014. Methods to detect, characterize, and remove motion artifact in resting state fMRI. Neuroimage 84, 320–341. https://doi.org/10.1016/j.neuroimage.2013.08.048.

Stroman, P.W., Ryner, L.N., 2001. Functional MRI of motor and sensory activation in the human spinal cord. Magn. Reson. Imag. 19, 27–32.

Tinnermann, A., Geuter, S., Sprenger, C., Finsterbusch, J., Büchel, C., 2017. Interactions between brain and spinal cord mediate value effects in nocebo hyperalgesia. Science 358 (6359), 105–108. https://doi.org/10.1126/science.aan1221.

Vahdat, S., Lungu, O., Cohen-Adad, J., Marchand-Pauvert, V., Benali, H., Doyon, J., 2015. Simultaneous brain–cervical cord fMRI reveals intrinsic spinal cord plasticity during motor sequence learning. PLoS Biol. 13 (6), 1–25. https://doi.org/10.1371/journal.pbio.1002186.

Weber, K.A., Chen, Y., Wang, X., Kahnt, T., Parrish, T.B., 2016a. Functional Magnetic Resonance Imaging of the Cervical Spinal Cord during Thermal Stimulation across Consecutive runs NeuroImage, vol 143. Elsevier, pp. 267–279. https://doi.org/10.1016/j.neuroimage.2016.09.015.

Weber, K.A., Chen, Y., Wang, X., Kahnt, T., Todd, B.P., 2016b. Lateralization of Cervical Spinal Cord Activity during an Isometric Upper Extremity Motor Task with Functional Magnetic Resonance Imaging. *NeuroImage*. Elsevier B.V., pp. 233–243. https://doi.org/10.1016/j.neuroimage.2015.10.014. January(125).

Weber, K., Bernadel-Huey, O., Chen, Y., Wang, X., Parrish, T., Mackey, S., 2017. Advanced spatial smoothing improves detection of cervical spinal cord activity with fMRI. In: Proceedings of the Annual Meeting of the Humain Brain Mapping Organization. Vancouver.

Wheeler-Kingshott, C.A., Stroman, P.W., Schwab, J.M., Bacon, M., Bosma, R., Brooks, J., Cadotte, D.W., Carlstedt, T., Ciccarelli, O., Cohen-Adad, J., Curt, A., Evangelou, N., Fehlings, M.G., Filippi, M., Kelley, B.J., Kollias, S., Mackay, A., Porro, C.A., Smith, S., Strittmatter, S.M., Summers, P., Thompson, A.J., Tracey, I., 2014. The Current State-Of-The-Art of Spinal Cord Imaging: applications, *NeuroImage*, vol 84. Elsevier Inc., pp. 1082–1093. https://doi.org/10.1016/j.neuroimage.2013.07.014

Woolrich, M., 2008. Robust group analysis using outlier inference. Neuroimage 41 (2), 286–301. https://doi.org/10.1016/j.neuroimage.2008.02.042.

Woolrich, M.W., Behrens, T.E.J., Beckmann, C.F., Jenkinson, M., Smith, S.M., 2004a. Multilevel linear modelling for FMRI group analysis using Bayesian inference. Neuroimage 21 (4), 1732–1747. https://doi.org/10.1016/j.neuroimage.2003.12.023.

Woolrich, M.W., Behrens, T.E.J., Smith, S.M., 2004b. Constrained linear basis sets for HRF modelling using Variational Bayes. Neuroimage 21 (4), 1748–1761. https://doi.org/10.1016/j.neuroimage.2003.12.024.

Woolrich, M.W., Ripley, B.D., Brady, M., Smith, S.M., 2001. Temporal autocorrelation in univariate linear modeling of FMRI data. Neuroimage 14 (6), 1370–1386. https://doi.org/10.1006/nimg.2001.0931.

Yakovenko, S., Mushahwar, V., Horst, V.V.A., Holstege, G., Prochazka, A., Vanderhorst, V., 2002. Spatiotemporal activation of lumbosacral motoneurons in the locomotor step cycle. J. Neurophysiol. 87, 1542–1553.

Yeganegi, H., Fathi, Y., Erfanian, A., 2018. Decoding hind limb kinematics from neuronal activity of the dorsal horn neurons using multiple level learning algorithm. Sci. Rep. 8 (1), 1–12. https://doi.org/10.1038/s41598-017-18971-x.

Yoshizawa, T., Nose, T., Moore, G.J., Sillerud, L.O., 1996. Functional magnetic resonance imaging of motor activation in the human cervical spinal cord. Neuroimage 4 (68), 174–182.